Recep Tayyip Erdoğan Üniversitesi Fen ve Mühendislik Bilimleri Dergisi, 6(3) 861-877 2025
Recep Tayyip Erdogan University Journal of Science and Engineering, 6(3) 861-877 2025
ISSN: 2687-2315 / E-ISSN: 2757-7686

Sintering-Driven Evolution of Phase, Microstructure, and Microstrain in Perlite-Containing Ceramics

Büşra Tansu CEYLAN [1], **Yunus Emre BENKLİ** [2] *

[1] Vocational School, Automotive Technology Program, Mudanya University, Bursa, Türkiye

[2] Department of Metallurgical and Materials Engineering, Faculty of Engineering, Atatürk University, Erzurum, Türkiye

Sorumlu Yazar/Corresponding Author
E-mail: yebenkli@atauni.edu.tr

Araştırma Makalesi/Research Article
Geliş Tarihi/Received: 05.09.2025
Kabul Tarihi/Accepted: 02.10.2025

Abstract

In this study, ceramic samples with perlite additions in the range of 0-50% were sintered at 1050, 1150, and 1250°C to investigate their effects on phase stability, microstructural evolution, and microstrain. The XRD patterns revealed that the quartz-dominant phase environment was preserved, and the broad amorphous hump at $2\theta \approx$ 8-16° was found for all groups. Scherrer analysis indicated that crystallite size reached its maximum (11-12 nm) in samples containing 10-20% perlite at 1150°C, whereas it decreased to as low as 2-3 nm at ≥40% perlite additions at 1250°C. The Williamson-Hall method demonstrated a pronounced increase in microstrain at 1250°C, peaking particularly around 40% perlite. SEM-based dark-field (%) analysis showed more compact and homogeneous structures at medium additions (20-40%), while higher additions tended to cause structural heterogeneity. Furthermore, microhardness measurements supported the observed structural trends. Overall, the findings suggest that the optimum microstructural features (10-20% perlite at 1150°C) were achieved through low microstrain, high crystallinity, and balanced crystallite size, while excessive perlite additions under advanced sintering conditions disrupted the morphology. These results contribute to defining the optimum perlite ratio in ceramic body design.

Keywords: Crystallinity index, crystallite size, microstrain, perlite-added ceramics, sintering.

Perlit Katkılı Seramiklerde Sinterleme Tabanlı Faz, Mikroyapı ve Mikrogerinim Evrimi

Öz

Bu çalışmada, %0-50 aralığında perlit katkılı seramik numuneler 1050, 1150 ve 1250°C'de sinterlenerek faz kararlılığı, mikroyapısal evrim ve mikrogerinim üzerindeki etkileri incelenmiştir. XRD desenleri, kuvars baskın faz ortamının korunduğunu ve $2\theta \approx$ 8-16° aralığındaki geniş amorf piklerin tüm gruplarda sürdüğünü göstermiştir. Scherrer analizi, 1150°C'de %10-20 perlit katkılı numunelerde kristalit boyutunun 11-12 nm ile maksimuma ulaştığını; 1250°C'de ≥%40 perlit katkılarında ise 2-3 nm'ye kadar gerilediğini ortaya koymuştur. Williamson-Hall yöntemi, 1250°C'de mikrogerinimin belirgin şekilde arttığını ve özellikle %40 perlit civarında maksimuma ulaştığını göstermiştir. SEM tabanlı koyu-alan (%) analizi, orta katkılarda (20-40%) daha kompakt ve homojen yapılar, yüksek katkılarda ise heterojenleşme eğilimi olduğunu ortaya koymuştur. Ek olarak, mikrosertlik ölçümleri de yapısal eğilimleri desteklemiştir. Bulgular birlikte değerlendirildiğinde, optimum mikroyapısal özelliklerin (%10-20 perlit, 1150°C) düşük mikrogerinim, yüksek kristalinite ve dengeli kristalit boyutu ile elde edildiği; yüksek perlit katkılarının ise ileri sinterleme altında morfolojiyi bozduğu sonucuna varılmıştır. Bu sonuçlar, seramik bünye tasarımında optimum perlit oranının belirlenmesine katkı sağlamaktadır.

Anahtar Kelimeler: Kristalinite indeksi, kristalit boyutu, mikrogerinim, perlit katkılı seramikler, sinterleme.

Cite as;
Ceylan, B.T and Benkli, Y.E (2025). Sintering-driven evolution of phase, microstructure, and microstrain in perlite-containing ceramics. *Recep Tayyip Erdogan University Journal of Science and Engineering,* 6(3), 861-877. Doi: 10.53501/rteufemud.1778513

1. Introduction

Türkiye holds approximately 15.8% of the world’s pumice reserves (≈2.8 billion tons) and 74% of perlite reserves, placing it in a strategically significant position on a global scale (Elmastas, 2012; Ceylan, 2019). However, these natural resources have not been sufficiently converted into high value-added products. Perlite, with a chemical composition of 70-75% SiO_2, 12-15% Al_2O_3, and alkali oxides (Na_2O, K_2O) (Civan, 2011; Bozkurt, 2013), rapidly loses its bound water upon heating due to its amorphous structure, leading to a volumetric expansion of 7-16 times (Mercan, 2021; Basar, 2023). This property enhances its importance as a lightweight, porous ceramic raw material with low thermal conductivity (Rekaa et al., 2019).

Although pumice has a chemical composition similar to ceramic raw materials, in industry it has mainly been used as a flux in glaze compositions instead of Na-feldspar (Poyraz et al., 2006), as an additive to reduce thermal conductivity in lightweight bricks (Gencel, 2015), and as a cement substitute or coarse aggregate in lightweight concrete (Hossain, 2004). Moreover, the blended use of pumice aggregate in lightweight concrete blocks has been particularly recommended (Binici, 2007; Ismail et al., 2018). In the ceramic industry, perlite has been utilized as a substitute for albite and has yielded positive results both in sanitaryware and in wall tile production with additions of 2-6% (Tarhan and Tarhan, 2018; Tarhan and Tarhan, 2022). Pumice, owing to its low cost, low density, and chemical composition similar to ceramic raw materials, is considered an important candidate for special ceramics. By partial sintering, porosity can be preserved while reducing heat and sound conductivity (Kuzugudenli and Zengin, 2004; Kuzugudenli, 2004). In addition, the high alkali content of perlite facilitates liquid-phase formation during sintering, enabling thermal conductivity values as low as 0.37 W/mK at additions up to 70%, although this simultaneously reduces the formability of the ceramic body (Rzepa et al., 2016). Koca (2024) reported that clay-pumice systems imparted vitreous ceramic body properties and yielded brighter color values in the final product. Similarly, Ozturk and Can (2023) demonstrated that micronized pumice can be incorporated into vitreous glaze compositions and applied in sanitaryware production without compromising technical properties.

In the ceramic industry, cold isostatic pressing (CIP) is a critical method since it reduces porosity and increases strength (Liu et al., 2016), while ensuring homogeneity in high-performance applications (Liu et al., 2014). Moreover, compared with hot isostatic pressing (HIP) and spark plasma sintering (SPS), CIP is a more cost-effective method that both improves product properties and reduces production costs (Lukianova, 2015). Ceramic processing methods vary depending on the characteristics and application areas of the raw materials. While traditional methods rely on high-temperature sintering, recent developments also encompass composite production, fine particle separation, and waste utilization. For instance, Durgut et al. (2025) reported the separation of halloysite and kaolinite below 38 µm using a dispersion–precipitation technique. Energy-efficient and optimized ceramic production has gained increasing importance in recent years. Methods such as microwave drying and in-situ sintering simulations enhance both performance and sustainability; in particular, microwave drying provides better homogeneity, higher mechanical strength, and significant energy savings compared to gas-based systems (Durgut, 2025).

In the literature, the effects of perlite on sintering have mostly been linked to phase transformations, porosity, or thermal behavior. However, systematic studies simultaneously addressing crystallite size and microstrain remain highly limited (Allen et al., 2009; Monshi et al., 2012; Kai et al., 2018; Fatimah et al., 2022; Gesing and Robben, 2024; Kawsar et al., 2024; Nusrat et al., 2024; Koca and Benkli, 2025). Addressing this gap is of great importance for both understanding structural mechanisms and advancing the design of improved ceramic materials. In this study, the combined effects of perlite content (0-50%) and sintering temperature (1050-1250°C) were systematically investigated in terms of phase stability, crystallinity index, crystallite size, microstrain (Williamson-Hall method), and SEM-based microstructural parameters. Thus, the role of perlite-temperature interaction on microstructure and crystalline was elucidated in detail. This approach contributes to a more comprehensive understanding of perlite addition in ceramics from both mechanical and structural perspectives.

2. Materials and Methods

2.1 Materials

Pumice and perlite raw materials were supplied from KALEBLOKBİMS quarries located in Erzurum/Pasinler, Türkiye. XRF results (Table 1 and Table 2) indicate that both raw materials contain high amounts of SiO_2 and significant levels of Al_2O_3, together with alkali oxides (Na_2O+K_2O) in sufficient amounts to promote glass phase formation. According to the TS 3673 standard, no organic matter was detected in the samples. This acidic, volcanic glass-dominated composition was considered as the fundamental input explaining the liquid-phase sintering behavior and morphological evolution observed in this study.

Table 1. XRF results of the pumice sample (%)

Component	wt.%	Component	wt.%
Na_2O	3.60	CaO	0.80
MgO	0.30	TiO_2	0.20
Al_2O_3	13.60	MnO	0.10
SiO_2	70.50	Fe_2O_3	1.90
P_2O_5	0.10	Loss on Ignition	4.30
K_2O	4.65		

Table 2. XRF results of the perlite sample (%)

Component	wt.%	Component	wt.%
Na_2O	4.12	CaO	0.46
MgO	0.17	TiO_2	0.08
Al_2O_3	12.40	MnO	0.06
SiO_2	72.70	Fe_2O_3	1.73
P_2O_5	<0.01	Loss on Ignition	3.35
K_2O	4.85		

2.2 Methods

The raw materials were ground using a Union Process Attritor mill to achieve a particle size of <400 μm. The powders were pre-pressed in steel molds (3×3×4 cm) and subsequently consolidated using an Ultra High Pressure MSE CIP Series cold isostatic press (CIP, 3000 bar capacity) at room temperature for 3 minutes. The specimens were sintered at 1050, 1150, and 1250°C for 10 minutes in a Protherm PTF series tube furnace (maximum capacity 1500°C). For clarity, the ceramic formulations were coded according to the perlite content. Samples without perlite were denoted as P00, while those with 10, 20, 30, 40, and 50 wt% perlite additions were coded as P10, P20, P30, P40, and P50, respectively. These codes are consistently used throughout the figures and tables to improve readability and comparison among groups.

Phase and scale-strain analyses were performed using a PANalytical X'Pert Pro XRD system with Cu Kα radiation. The patterns obtained were evaluated after area normalization, with selected peak windows and the amorphous hump taken into consideration. Crystallite size was calculated using the Scherrer equation, while microstrain (ε) was determined using the Williamson-Hall (W-H) approach.

Microstructural examinations were conducted with a ZEISS EVO LS10 SEM. Image analysis employed the dark-field area fraction (%) metric based on Otsu thresholding, optimized for intra-detector comparison. Microhardness measurements were carried out using a Shimadzu HMV-G21S microhardness tester as a complementary mechanical indicator.

This methodological package enabled direct support of the critical trends observed in the study, such as the large crystallite size and low ε for 10-20% perlite at 1150°C, and crystallite refinement with increased heterogeneity at ≥40% perlite under 1250°C sintering.

Note: Certain limitations exist in the methods used in this study. The crystallinity index (CI) provides only a relative indicator and not an absolute phase fraction. Scherrer analysis estimates crystallite size but does not account for strain-induced peak broadening. The Williamson-Hall method offers the advantage of separating size and strain contributions, yet the results are sensitive to peak selection and background correction. Similarly, the SEM-based dark-field (%) metric does not represent absolute porosity; it is only valid for relative comparisons within the same detector configuration. The findings of this study were interpreted with these limitations in mind.

3. Results and Discussion

This section presents the effects of perlite content (P00-P50) and sintering temperature (1050-1250°C) on phase composition, microstructure, and scale-strain parameters. The results are sequentially discussed in terms of area-normalized XRD (Scherrer/W-H) → SEM/EDS morphology → microhardness measurements.

Figure 1 compares the area-normalized XRD patterns of samples with perlite contents ranging from P00 to P50, sintered at 1050, 1150, and 1250°C. Area normalization ensures that the total integral of each curve is equalized, thereby allowing reliable comparison of peak shapes and positions. However, it should be noted that absolute crystalline/amorphous fractions cannot be extracted from this method.

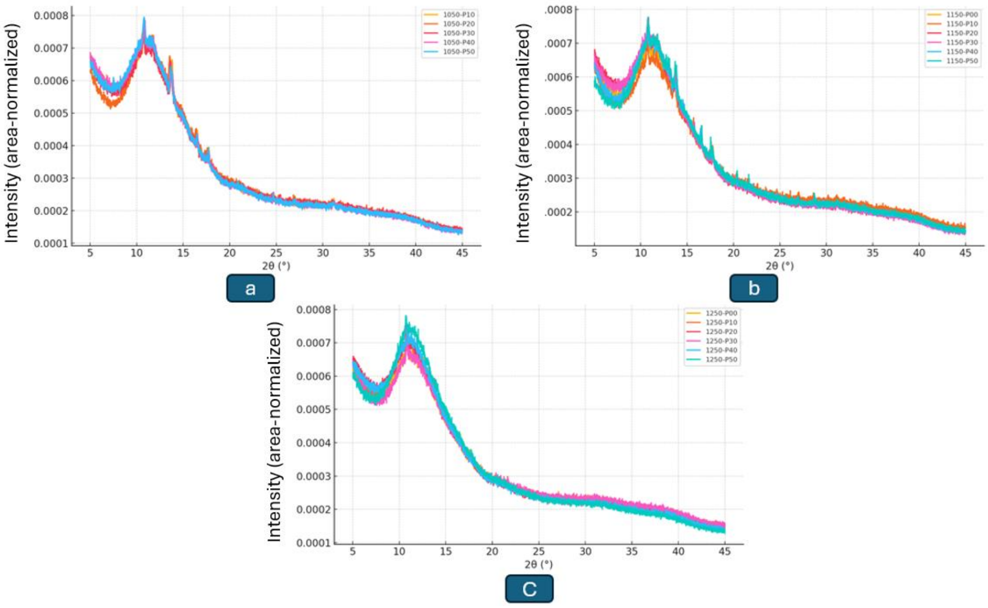

Figure 1. Area-normalized XRD patterns: (a) 1050°C, (b) 1150°C, (c) 1250°C (P00-P50).

Figure 1a shows that the XRD patterns of P00-P50 samples largely overlap, with low-intensity reflections observed at 2θ ≈ 20.8-21.0°, 26.5-26.8°, 36-37°, and 39-41°, corresponding to α-quartz/cristobalite. The broad amorphous hump in the 2θ ≈ 8-16° range indicates the presence of glassy/amorphous phases. Since the curves were area-normalized, peak intensities are suitable only for relative comparison; determination of absolute phase fractions would require internal-standard Rietveld refinement or peak fitting. The high similarity among patterns suggests that perlite addition has only a limited effect on the phase inventory, while the observed differences are more likely associated with viscous flow and microstructural evolution driven by sintering conditions.

Figure 1b (1150°C) again shows substantial overlap among the patterns, with low-intensity reflections at 2θ ≈ 20.8-21.0°, 26.5-26.9°, 31-33°, 35-37°, 39-41°, and ~43°, consistent with α-quartz, feldspar, and trace oxide phases. The amorphous hump in the 2θ ≈ 8-16° region supports the continuity of the glassy phase. The mullite window (≈16.4°) lies very close to the amorphous hump, and the minor fluctuations observed in this region are sensitive to background modeling rather than indicative of distinct crystalline phases.

Figure 1c (1250°C) demonstrates that the diffraction patterns of perlite-added samples converge even further, with reflections at 2θ ≈ 20.8-21.1°, 26.5-26.9°, and 33-35° corresponding to α-quartz along with minor feldspar/oxide phases. The persistence of the amorphous hump at 2θ ≈ 8-16° confirms the continuity of the glassy phase. The increased overlap among patterns at higher temperatures can be attributed to enhanced viscous flow and stabilization of the glassy matrix.

Overall, the results confirm the preservation of a quartz-dominated phase environment, while the influence of perlite addition is manifested primarily through glassy phase formation and viscous flow behavior. Minor irregular fluctuations in the amorphous hump region are more indicative of variability in the glassy phase content rather than the emergence of new crystalline phases. This interpretation is consistent with previous reports highlighting the role of perlite in modulating sintering behavior in sanitary ceramics (Tarhan and Tarhan, 2022) and wall tile production (Tarhan and Tarhan, 2018).

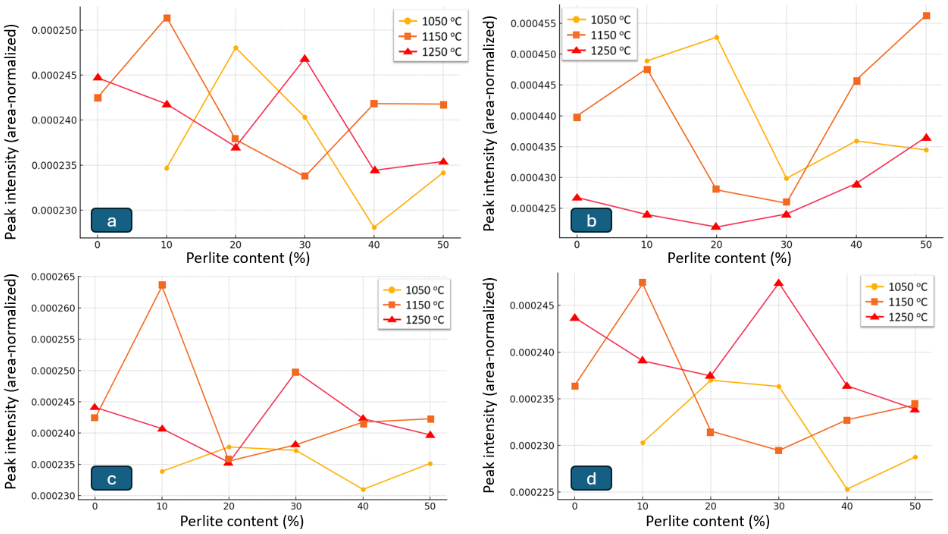

Figure 2. Normalized peak intensity as a function of perlite addition at different temperatures (1050, 1150, 1250°C): (a) Quartz 26.6°, (b) Mullite 16.4°, (c) Mullite 26.0°, (d) Feldspar 27.5-28.5°.

Figure 2 illustrates the variation of peak intensities with perlite content (%) within phase-specific 2θ windows. In the quartz window (2θ ≈ 26.6°), the intensities fluctuated within a narrow range across all sintering temperatures, without exhibiting a clear trend. In the mullite window (2θ ≈ 16.4°), a local minimum was observed around P20, followed by an increase toward P40-P50; however, since this region lies close to the amorphous hump, the results are sensitive to background modeling. In the mullite window (2θ ≈ 26.0°), no consistent trend was identified across temperatures; a local maximum appeared near P30 at 1250°C, whereas a decreasing tendency was observed at 1150°C. In the feldspar window ($2\theta \approx 27.5$-$28.5°$), a general decreasing trend with increasing perlite addition became particularly pronounced at 1250°C, while a local peak was recorded at P30 at 1150°C.

Overall, these limited and irregular intensity trends indicate that perlite addition influences primarily the glassy phase content and microstructural evolution rather than promoting the formation of new crystalline phases. This interpretation is consistent with earlier reports highlighting that variations in glassy phase content modulate sintering behavior through viscous flow and liquid-phase formation (Rahaman, 2003; Carty and Senapati, 2005). The minor fluctuations within the amorphous hump region (Figure 3) further confirm that the observed changes are more closely associated with glass/crystal ratio variability than with the emergence of new crystalline phases. Therefore, Figure 2 demonstrates that perlite addition exerts only a limited effect on phase transformation, while the main differences arise from glassy phase proportion and temperature-dependent evolution, in agreement with prior studies (Tarhan and Tarhan, 2018; 2022).

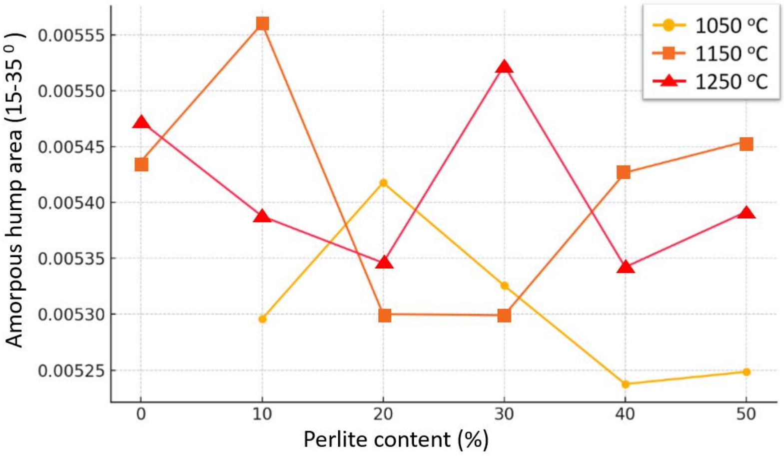

Figure 3. Amorphous hump area (15-35° 2θ) versus perlite content at 1050, 1150, and 1250°C. (The curves represent the relative amorphous index (∫I_norm d2θ) derived from area-normalized XRD patterns. The values are intended for comparison only and do not provide an absolute amorphous fraction.)

The amorphous hump area (∫I_norm d2θ) in the range of $2\theta = 15$-$35°$ was calculated from the area-normalized XRD patterns, and its relative variation with perlite content is presented in Figure 3. At all three temperatures, the amorphous contribution was preserved; however, the variation with perlite (%) was weak and not distinctly monotonic. At 1050°C, a shallow maximum appeared around P20, followed by a decrease toward P40-P50, where a minimum was observed. At 1150°C, a relatively high value was recorded at P10, followed by a minimum at P20-P30, and then a renewed increase toward P40-P50, producing a U-shaped profile. At 1250°C, a minimum was observed near P20, followed by a local maximum at P30. The overall fluctuations were small, with deviations remaining below 5% around the average.

These limited and non-monotonic variations demonstrate that the effect of perlite addition in ceramic bodies arises primarily from fluctuations in the glassy phase content rather than the formation of new crystalline phases. In particular, the U-shaped profile observed at 1150°C suggests transient fluctuations in the balance between glassy and crystalline phases during sintering. Similarly, the minimum-maximum oscillation at 1250°C can be explained by the interplay between quartz-mullite transformations and viscous flow at elevated temperatures. These findings are consistent with previous studies reporting that perlite primarily modulates sintering behavior while maintaining the continuity of the amorphous phase (Tarhan and Tarhan, 2018; Tarhan and Tarhan, 2022). Figure 3 further confirms that the phase assemblage remains quartz-dominated regardless of perlite content, with the observed variations being primarily associated with glassy phase fluctuations. Moreover, perlite has been reported to enhance sinterability and modulate pore morphology (Kayacı, 2020). Indeed, it has also been shown that perlite addition can reduce the sintering temperature (Idrissi et al., 2023), supporting its potential role in promoting microstructural homogeneity.

To complement this limited and non-monotonic amorphous variation, peak broadening in crystalline regions was analyzed using the Williamson-Hall (W-H) method to obtain microstrain (ε) values. Although the diffraction patterns were area-normalized, W-H analysis relies on FWHM and is therefore unaffected by this normalization. The evolution of ε as a function of perlite content (0-50%) and sintering temperature (1050-1250°C) is presented in Figure 4.

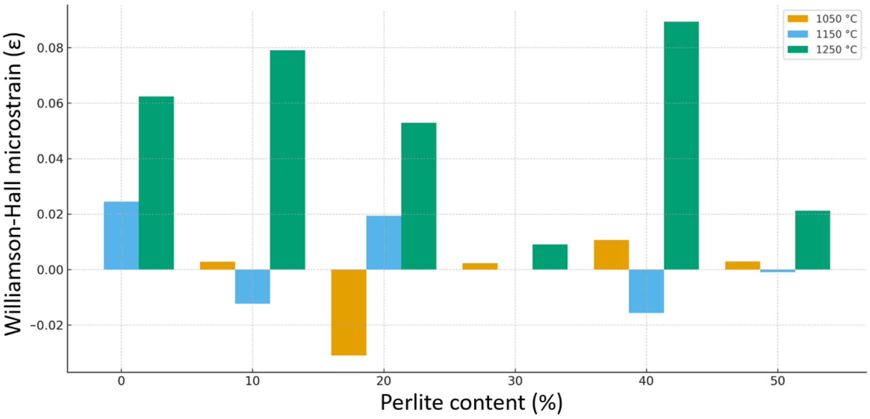

Figure 4. Variation of microstrain (ε) values calculated by the Williamson-Hall method as a function of perlite content at different sintering temperatures (1050°C, 1150°C, and 1250°C).

Figure 4 presents the microstrain (ε) values calculated using the Williamson-Hall (W-H) method for different perlite additions. At 1050°C, ε values remained at low levels and no distinct trend emerged with increasing perlite content. At 1150°C, a limited increase was observed in the P10-P20 range, followed by a partial decrease at higher perlite contents. At 1250°C, however, the microstrain values increased markedly, reaching a maximum particularly around P40. This behavior indicates that higher temperatures combined with higher perlite additions promote the accumulation of lattice strain within the crystalline structure.

The increase in microstrain can be attributed to lattice mismatches generated during quartz-mullite transformations and to thermal expansion mismatches between glassy and crystalline phases. Although the increased glassy phase content at higher temperatures provides partial relaxation through viscous flow, it could not fully compensate for the stress concentrations within crystalline phases. Indeed, changes in the slopes of W-H plots further support this interpretation. Consistent with earlier reports by Monshi et al. (2012) and Allen et al. (2009), elevated microstrain values are directly linked to crystallite refinement and lattice distortion. Therefore, Figure 4 demonstrates that high temperatures and high perlite additions tend to destabilize the crystalline structure by increasing microstrain, whereas intermediate perlite-temperature combinations provide a more balanced lattice configuration.

The effect of perlite content (%) and temperature on the crystallinity index (CI) is presented in Figure 5. CI is a relative measure based on the ratio of crystalline peak intensities to the amorphous background within selected 2θ windows, increasing as the proportion of crystalline phases rises. Following the assessment of defect/strain contributions via W-H analysis, CI was introduced as a proxy indicator of phase fraction and its variation with perlite (%) was evaluated. It should be noted that CI does not represent an absolute crystalline percentage and remains sensitive to background modeling. Taken together, ε captures the defect/strain state, while CI provides complementary insight into the crystalline-amorphous balance as a relative quantitative trend.

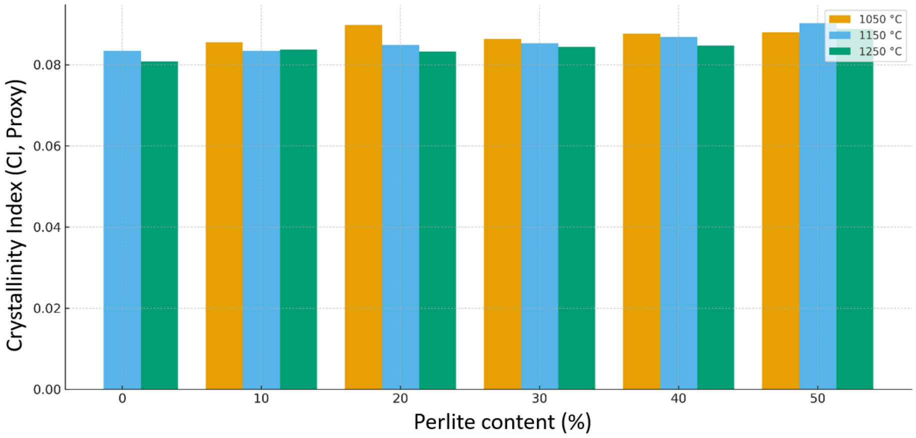

Figure 5. Variation of the crystallinity index (CI, relative measure) as a function of perlite content at different sintering temperatures (1050, 1150, and 1250°C).

Figure 5 shows the variations in the crystallinity index (CI, proxy) as a function of perlite content. At 1050°C, CI values fluctuated within the range of 0.084-0.090, reaching a local maximum around P20, followed by a decreasing tendency at higher perlite additions. At 1150°C, CI exhibited a relatively steady increase, attaining its maximum at P50. At 1250°C, the lowest CI values were recorded at low additions (P0-P10), while a gradual increase was observed with higher perlite contents, reaching approximately 0.089 at P50.

These findings indicate that perlite addition does not exert a direct linear effect on crystallinity; instead, the trends emerge from the combined influence of both temperature and perlite content. The local maxima observed at intermediate additions (particularly around P20 at 1050°C) suggest transient densification of crystalline phases, whereas the crystallinity increase at higher additions (P40-P50 at 1150-1250°C) can be attributed to enhanced continuity of crystalline domains within the glassy matrix.

Similar observations have been reported in the literature, where perlite addition was found to modulate the crystalline-amorphous balance and thereby influence sintering behavior in ceramic systems (Tarhan and Tarhan, 2018; Tarhan and Tarhan, 2022). Accordingly, Figure 5 demonstrates that the evolution of crystallinity is shaped by the coupled effects of perlite ratio and sintering temperature, with the optimum crystalline-amorphous balance achieved at 1150°C with medium-to-high perlite contents.

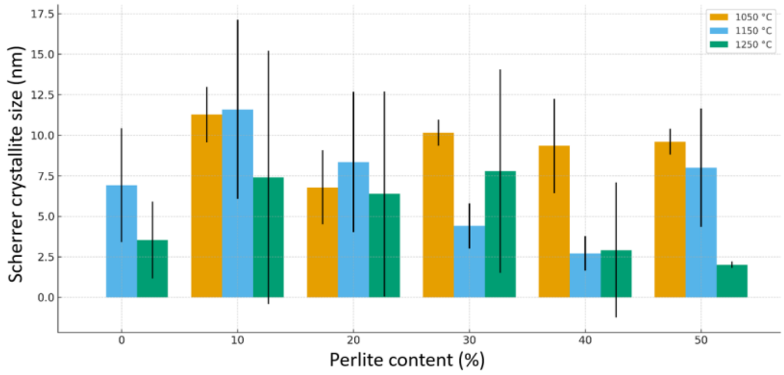

Figure 6. Scherrer crystallite size (D_Sch) versus perlite content (%) at 1050, 1150, and 1250°C.

Figure 6 presents the crystallite sizes calculated using the Scherrer equation. At 1050°C, crystallite sizes ranged between 7-10 nm, with the P10 sample reaching a maximum of ~11.5 nm. At 1150°C, a peak size of ~11-12 nm was observed at P10, followed by a decrease to 4-5 nm at P30, and then a partial recovery to ~8 nm at P50. At 1250°C, crystallite sizes remained generally low; values of 6-8 nm were recorded for P10-P30, while P40 and P50 exhibited pronounced refinement down to 2-3 nm.

This trend indicates that intermediate perlite additions combined with moderate temperatures promote crystallite growth, whereas high perlite contents at elevated temperatures lead to crystallite refinement through a dissolution-recrystallization mechanism. The pronounced reduction observed at 1250°C is associated with increased glassy phase formation and quartz-feldspar interactions. Similar behavior has been reported in the literature, where crystallite refinement at high temperatures was found to parallel increases in microstrain (Allen et al., 2009; Monshi et al., 2012). Accordingly, Figure 6 demonstrates that optimum crystallite sizes, according to Scherrer analysis, are achieved at 1150°C with 10-20% perlite additions, whereas high additions under high-temperature sintering conditions destabilize the crystalline network, resulting in significantly smaller crystallites. Comparable crystallite refinement at elevated sintering temperatures has also been reported by Koca and Benkli (2025).

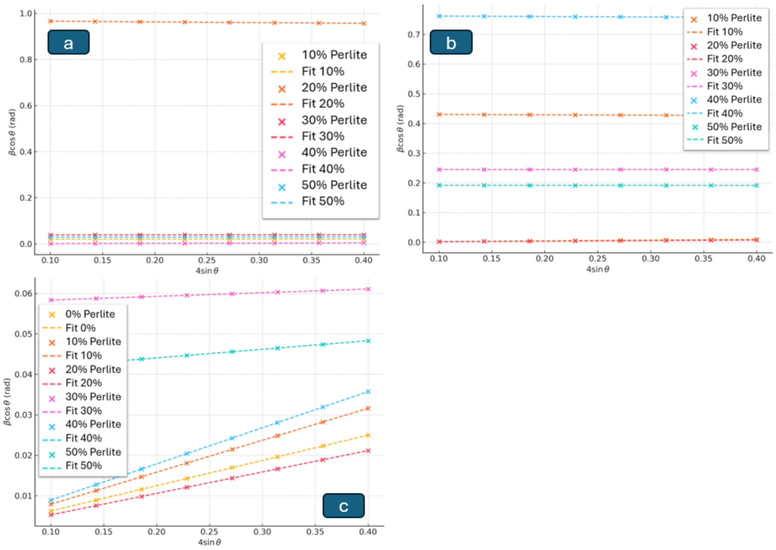

Figure 7. Line broadening–diffraction angle (βcosθ-4sinθ) relationships and linear regressions obtained by the Williamson-Hall (W-H) method: (a) 1050°C, (b) 1150°C, (c) 1250°C perlite-containing samples.

The microstrain (ε) values presented in Figure 4 are further corroborated by the Williamson-Hall (W-H) plots shown in Figure 7, which display the W-H linear fits obtained at different sintering temperatures and perlite contents. At 1050°C, the slopes were nearly zero and the lines appeared almost horizontal, indicating low microstrain and a limited contribution of size broadening. At 1150°C, the plots exhibited a more regular distribution, with higher intercept values in the P10-P20 range, suggesting larger crystallite sizes. At 1250°C, the slopes increased significantly, with strain effects becoming dominant, particularly in the P40 sample. This result highlights that while crystallite size decreased (Figure 6), microstrain contributions became more pronounced at high temperature and high perlite additions.

Although the regression lines suggest good agreement, the actual reliability is constrained by the limited 2θ range and peak overlap, as frequently reported in the literature (Monshi et al., 2012; Kawsar et al., 2024). Thus, despite the methodological limitations, Figure 7 confirms that strain dominance increases under high-temperature and high-perlite conditions, whereas crystallite growth is more pronounced at intermediate perlite-temperature combinations. It should be noted that both the Scherrer and Williamson–Hall approaches provide only approximate crystallite sizes and strain values, being strongly influenced by instrumental broadening and peak profile assumptions.

To further investigate the origin of these differences, SEM morphologies and image-derived dark-field area fractions (%) are presented in Figures 8-10. It should be noted that the dark-field (%) metric does not represent absolute porosity; values were calculated using Otsu thresholding after a 12% sub-band correction and were interpreted as relative indicators of surface porosity. Comparisons were carried out within the same detector configuration (1050/1250: SE2; 1150: InLens). For each perlite group, the single image closest to the median was selected, and the distributions were quantitatively supported by box plots (median, IQR).

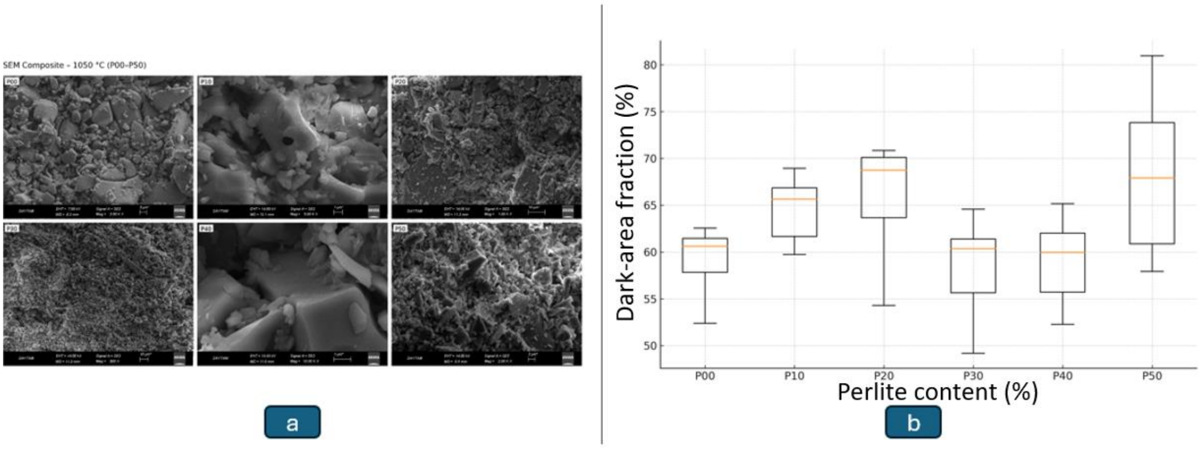

Figure 8. Microstructural and quantitative analysis of perlite-containing ceramics sintered at 1050°C. (a) SEM images of perlite-containing samples at different perlite ratios (P00-P50), (b) box plots showing the variation of dark-area fraction (%) with perlite content.

Figure 8 presents the SEM micrographs and dark-field area fraction (%) box plots of the samples sintered at 1050°C. In the P00 specimen, large and discontinuous pores dominate the microstructure. In the P20 sample, the matrix appears more compact; however, the box plot indicates a relatively higher dark-field fraction. The P30 sample exhibits both SEM images and box-plot data consistent with a lower dark-field fraction, pointing to a more homogeneous matrix structure. In contrast, the P50 sample shows re-enlarged and discontinuous pores due to the increased glassy phase, accompanied by a broader distribution in the box plot.

These findings reveal that perlite addition does not alter the pore structure in a strictly linear manner; rather, intermediate additions (particularly P30) promote homogenization, while higher additions (P50) increase heterogeneity. Similar results have been reported in the literature, where perlite at low temperatures accelerates glassy phase formation and facilitates densification, but excessive additions lead to renewed pore continuity within the glassy matrix (Tarhan and Tarhan, 2018; Tarhan and Tarhan, 2022). Accordingly, Figure 8 demonstrates that at 1050°C, the optimum pore structure is achieved in the P30 sample, whereas further addition to P50 results in structural degradation. The relatively homogeneous structure observed in the P20–P30 samples at 1050 °C may be associated with enhanced sinterability at lower temperatures, as also discussed in classical sintering studies reporting that intermediate glassy phase formation can promote densification even under suboptimal firing conditions (Kingery et al., 1976; Barsoum, and Barsoum, 2002).

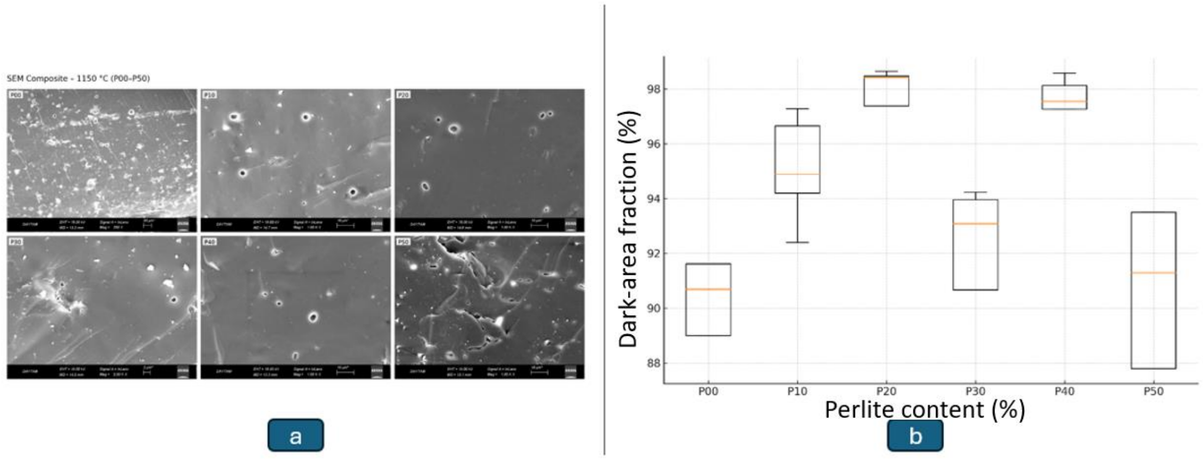

Figure 9. Microstructural and quantitative evaluation of perlite-containing ceramics sintered at 1150°C. (a) InLens SEM images of perlite-containing samples (P00-P50), (b) box plots showing the variation of dark-area fraction (%) with perlite content.

Figure 9 presents the InLens SEM micrographs and dark-field area fraction (%) box plots of the samples sintered at 1150°C. In the P00 specimen, the pore area is extensive and irregular. In the P20-P40 samples, the surfaces appear more compact and homogeneous, with increased dark-field fractions but narrow interquartile ranges (IQR), indicating low variation. This suggests that intermediate perlite additions reduce pore continuity and promote a more uniform matrix structure. In contrast, the P50 sample exhibits pronounced flow ridges and shrinkage marks due to the increased glassy phase, accompanied by a broader dark-field distribution and renewed heterogeneity.

These findings indicate that under optimum sintering conditions (1150°C), intermediate perlite additions enhance densification behavior, whereas excessive addition disrupts homogeneity owing to the surplus glassy phase. Similar observations have been reported in the literature, where controlled perlite contents were shown to improve sintering efficiency, while higher levels led to viscous flow that compromised matrix integrity (Tarhan and Tarhan, 2018; Tarhan and Tarhan, 2022). Accordingly, Figure 9 demonstrates that the optimum pore architecture at 1150°C is achieved in the P20-P40 samples, while P50 addition increases heterogeneity and weakens the compact structure.

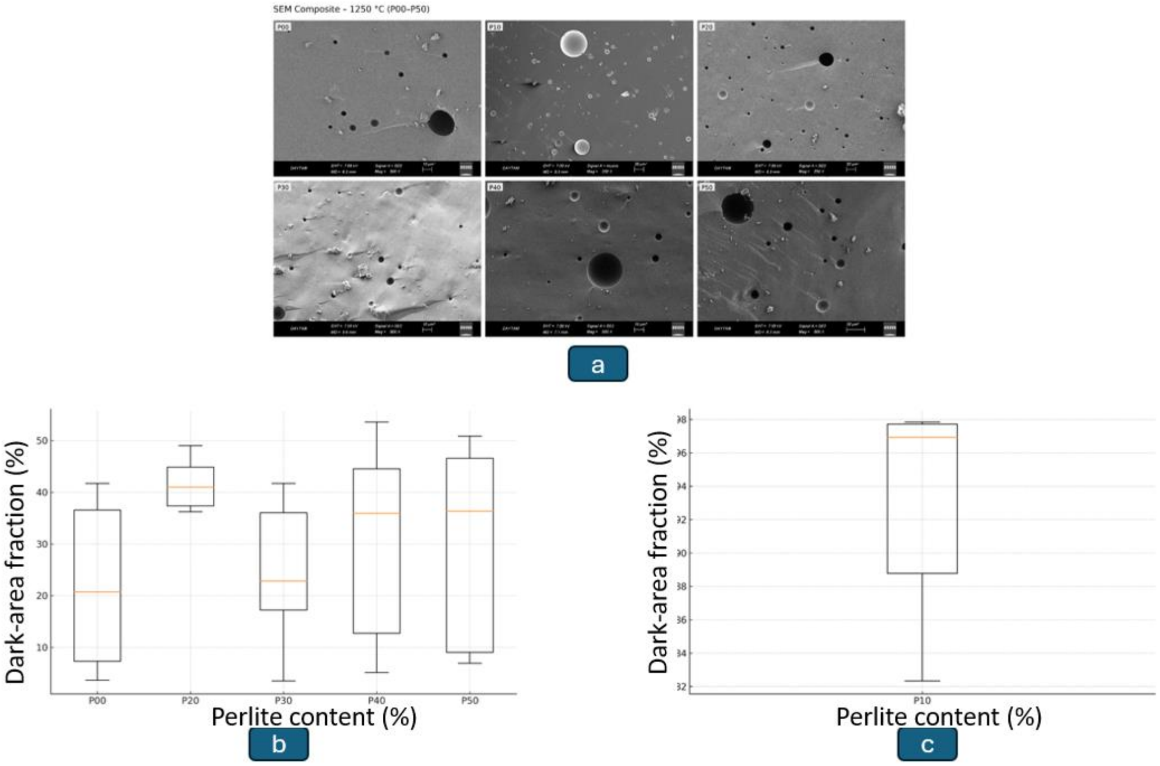

Figure 10. SEM and dark-area (%) analyses of perlite-containing samples at 1250°C: (a) SEM image panels of P00-P50 composites (SE2 detector, lower band cropped), (b) box plots showing the relationship between dark-area fraction (%) and perlite content (%) (SE2), (c) box plot of dark-area fraction (%) for the P10 sample obtained with the InLens detector (lower band cropped).

Figure 10 presents the SEM micrographs and dark-field area fraction (%) analyses of the samples sintered at 1250°C. In the P00 specimen, the pore structure appears irregular and discontinuous. In the P20-P30 samples, pores became smaller and the distribution more homogeneous. By contrast, in the P40 and especially P50 samples, pores re-enlarged, the distribution became more heterogeneous, and the interquartile range (IQR) of the dark-field values broadened. These results indicate that high perlite additions under advanced sintering conditions disrupt matrix integrity and increase pore continuity.

In the SE2-based box plots (Figure 10b), the P20-P30 samples exhibited the lowest variation, reflecting a more homogeneous structure. In the P40-P50 samples, however, variation increased and pore heterogeneity became more pronounced. In the InLens measurements (Figure 10c), the P10 sample stood out as one of the most compact specimens, with a dark-field fraction of ~95%. It should also be emphasized that the dark-field area fraction method provides only relative comparisons of pore distribution and does not represent absolute porosity values.

These findings demonstrate that elevated temperature accelerates viscous flow and increases glassy phase formation, which, beyond certain perlite levels, leads to renewed pore continuity. Similar trends have been reported in the literature, where high temperatures and high perlite additions resulted in re-enlarged pores and increased matrix heterogeneity (Tarhan and Tarhan, 2018; Tarhan and Tarhan, 2022). Accordingly, Figure 10 shows that at 1250°C, intermediate additions (P20-P30) provide relatively more homogeneous structures, whereas higher additions (P40-P50) deteriorate the pore architecture.

These microstructural observations were further supported by microhardness measurements, serving as a complementary mechanical indicator.

Table 3 presents the microhardness (HV0.1) values, standard deviations (SD), and coefficients of variation (CV%) of the perlite-containing ceramics sintered at 1050–1250 °C. At 1050 °C, microhardness values ranged from 318–398 HV, reflecting the persistence of porosity. At 1150 °C, values increased significantly (610–670 HV), with particularly favorable results in the P10–P20 range, indicating optimum densification. At 1250 °C, high average hardness was retained, but the standard deviations broadened, suggesting increased heterogeneity due to grain growth and viscous flow. The CV% values remained below 5% for all samples, confirming that the measurements were generally consistent and reproducible while still reflecting natural microstructural variations.

Table 3. Microhardness values (HV0.1), standard deviations (SD), and coefficients of variation (CV%) of perlite-containing ceramic samples sintered at different temperatures.

Sample	Mean HV	SD	CV%
1050P00	372.67	5.51	1.48
1050P10	378.33	2.31	0.61
1050P20	397.67	3.06	0.77
1050P30	360.33	3.21	0.89
1050P40	343.33	5.51	1.60
1050P50	318.33	4.93	1.55
1150P00	611.67	3.21	0.52
1150P10	633.67	3.06	0.48
1150P20	652.33	4.16	0.64
1150P30	634.67	4.04	0.64
1150P40	609.67	3.21	0.53
1150P50	615.67	5.03	0.82
1250P00	672.67	3.06	0.45
1250P10	653.00	6.11	0.94
1250P20	660.33	4.51	0.68
1250P30	632.33	2.52	0.40
1250P40	620.67	6.66	1.07
1250P50	609.67	8.08	1.33

HV0.1 values were measured under a 100 gf load, and each result represents the mean of three repeated measurements. Standard deviation (SD) indicates the dispersion of the measurements, while the coefficient of variation (CV%) reflects relative variability with respect to the mean. CV% values remained below 5% for all samples, indicating that the measurements were consistent and reproducible.

In this study, it was also observed that high perlite additions and sintering at 1250 °C produced fine-crystallite, glass-rich structures. Although such heterogeneous and strain-intensive bodies are disadvantageous in terms of structural integrity, the literature reports that porous or heterogeneous microstructures may be beneficial for certain applications, such as thermal shock resistant ceramics (due to stress dissipation through pores) (Lu and Fleck, 1998), lightweight thermal insulation materials (owing to reduced thermal conductivity) (Chen et al., 2023), catalyst supports and filtration membranes (because of their high surface area and permeability) (Wang et al., 2024), and even bio-ceramic scaffolds (facilitating fluid transport and tissue growth) (Abbasi et al., 2020). In particular, ceramics designed for thermal shock resistance or specialized fine-crystallite structures may deliberately exploit such microstructural features (Kingery et al., 1976; Barsoum, and Barsoum, 2002).

In addition, while structural uniformity decreases at higher perlite contents, such heterogeneous architectures may provide potential advantages for specific applications requiring improved thermal shock resistance. Finally, it should be highlighted that the dark-field method reflects relative porosity trends rather than absolute values, and that accurate phase quantification would require Rietveld refinement.

4. Conclusions

The XRD patterns confirmed that quartz remained the dominant phase regardless of perlite addition, while the continuity of the amorphous phase was preserved. The increased convergence of the diffraction patterns with rising temperature indicated that microstructural variations, rather than the formation of new phases, became more prominent.

Scherrer analysis revealed that crystallite size reached its highest values (~11-12 nm) in samples with 10-20% perlite addition at 1150°C, whereas significant refinement to 2-3 nm occurred at ≥40% additions at 1250°C. The Williamson-Hall analysis demonstrated that microstrain increased in all groups at 1250°C, reaching maximum values particularly around 40% perlite. This suggests that phase transformations and variations in the glass/crystal ratio intensified lattice-level stresses.

SEM examinations showed that bodies with low-to-medium perlite additions developed more compact structures, with pore size distributions narrowing and trending toward homogeneity. By contrast, high perlite contents led to increased porosity and broader pore size distributions due to excess glassy phase, thereby promoting heterogeneity. Notably, the P20-P40 groups at 1150°C exhibited uniform morphologies with narrow distribution ranges. Conversely, at 1250°C, high perlite contents resulted in broadened distributions and surface irregularities, indicating a loss of structural uniformity.

Overall, while perlite addition and sintering temperature did not fundamentally alter the phase composition, they exerted pronounced effects on crystallinity, microstrain, and morphology. The findings suggest that the optimum condition is achieved with 10-20% perlite addition at 1150°C, under which homogeneous and mechanically robust ceramic bodies are obtained. In contrast, higher additions and sintering at 1250°C produced fine-crystallite but heterogeneous structures, posing risks to structural integrity.

It should be noted that the XRD patterns were normalized to enable relative phase comparisons. However, absolute phase quantification cannot be obtained by this method; Rietveld refinement would be required for accurate quantitative analysis.

Author Contributions

This article is derived from the Master's thesis entitled *"Investigation of the Usability of Pumice and Perlite from the Erzurum Region in the Ceramic Industry"*. Ceylan, B.T**:** Experimental work, XRD and SEM analyses, visualization, writing - original draft; Benkli, Y, E**:** Conceptualization, methodology, data interpretation, writing - review and editing, validation. All authors have read and approved the final version of the manuscript.

Ethical Statement

The authors declare that no studies involving human participants or animals were conducted by the authors for this article.

Conflict of Interest

The authors declare that there is no conflict of interest.

Funding

This research did not receive any specific grant from funding agencies in the public, commercial, or not-for-profit sectors.

References

Abbasi, N., Hamlet, S., Love, R. M., & Nguyen, N.-T. (2020). Porous scaffolds for bone regeneration. *Journal of Science: Advanced Materials and Devices, 5*(1), 1–9. https://doi.org/10.1016/j.jsamd.2020.01.007

Allen, W.B., Kenneth, O., Thomas, R., Ignatius, Y.C. (2009). On the estimation of average crystallite size of zeolites from the Scherrer equation: A critical evaluation of its application to zeolites with one-dimensional pore systems. *Microporous and Mesoporous Materials*, 117(1–2), 75-90. https://doi.org/10.1016/j.micromeso.2008.06.010

Barsoum, M., Barsoum, M.W. (2002). Fundamentals of Ceramics (1st ed.). CRC Press, 9780429194924, Boca Raton, 624. https://doi.org/10.1201/b21299

Basar, F.S. (2023). Investigation of the Contribution of Perlite in Ceramic Mud and its Applications. Thesis (M.Sc.), Sakarya University, Institute of Social Sciences, Türkiye.

Benkli, Y.E., Koca, K. (2024). Suitability and characterization of pumice, bauxite, and ferrochrome slag as alternative raw materials in vitrified ceramic industry. *Physicochemical Problems of Mineral Processing*, 60(2), 187967. https://doi.org/10.37190/ppmp/187967

Binici, H. (2007). Effect of crushed ceramic and basaltic pumice as fine aggregates on concrete mortars properties. *Construction and Building Materials*, 21(6), 1191-1197.

https://doi.org/10.1016/j.conbuildmat.2006.06.002

Bozkurt, N. (2013). The effect of high temperature on concrete containing perlite powder. *SDU International Technologic Science*, 5(1), 87-93.

Carty, W., Senapati, U. (2005). Porcelain-raw materials, processing, phase evolution, and mechanical behavior. *Journal of the American Ceramic Society*. 81(1), 3-20. https://doi.org/10.1111/j.1151-2916.1998.tb02290.x.

Ceylan, B.T. (2019). Investigation of Pumice and Perlite Extracted in Erzurum Region for the Usability in Ceramics Industry. Thesis (M.Sc.), Atatürk University, Institute of Science and Technology, Türkiye.

Chen, A., Li, L., Ren, W., Wang, C., & Wang, Q. (2023). Enhancing thermal insulation and mechanical strength of porous ceramic through size-graded MA hollow spheres. *Ceramics International, 49*(20), 33247–33254. https://doi.org/10.1016/j.ceramint.2023.08.033

Civan, L. (2011). Uses of Pumice as a Glaze Composition and Investigations. Thesis (M.Sc.), Anadolu University, Institute of Science and Technology, Türkiye.

Durgut, E. (2025). Evaluation of the use of microwave energy on green floor/wall tile drying process. *Drying Technology*, 43(5), 937–948.

https://doi.org/10.1080/07373937.2025.2474156

Durgut, E., Çavdar, Y.E., Çınar, M., Yavuz, O., Özdemir, O. (2025). Fine-size separation of halloysite, kaolinite, and quartz minerals as binary systems using dispersion and sedimentation methods. *Physicochemical Problems of Mineral Processing*, 61(3), 203-225. https://doi.org/10.37190/ppmp/203225

Elmastas, N. (2012). A mine becoming increasingly important for economy of Turkey: pumice. *The Journal of International Social Research*, 5(23), 197–206.

Fatimah, S., Ragadhita, R., Husaeni, D.F., Nandiyanto, A.B.D. (2022). How to calculate crystallite size from X-Ray Diffraction (XRD) using Scherrer Method. *ASEAN Journal of Science and Engineering*, 2(1), 65-76. https://doi.org/10.17509/ajse.v2i1.37647

Gencel, O. (2015). Characteristics of fired clay bricks with pumice additive. *Energy and Buildings*, 102, 217–224. https://doi.org/10.1016/j.enbuild.2015.05.031

Gesing, T.M., Robben, L. (2024). Determination of the average crystallite size and the crystallite size distribution: the envelope function approach EnvACS. *Journal of Applied Crystallography*, 57(5), 1466-

1476. https://doi.org/10.1107/S1600576724007362

Hossain, K.M.A. (2004). Properties of volcanic pumice based cement and lightweight concrete. *Cement and Concrete Research*, 34(2), 283–291.

https://doi.org/10.1016/j.cemconres.2003.08.004

Idrissi, D.E.M., Elidrissi, Z.C., Achiou, B., Ouammou, M., Younssi, S.A. (2023). Fabrication of low-cost kaolinite/perlite membrane for microfiltration of dairy and textile wastewaters. *Journal of Environmental Chemical Engineering,* 11(2), 109281.

https://doi.org/10.1016/j.jece.2023.109281

Ismail, A.I.M., Souaya, E.R., Fathy, M., Abd El-Hakeem A. (2018). Production of lightweight concretes from pumice/bentonite mix. *Geotechnical and Geological Engineering,* 36, 581-588. https://doi.org/10.1007/s10706-017-0348-z

Kai, H., Nuofu, C., Congjie, W., Lishuai, W., Jikun, C. (2018). Method for determining crystal grain size by X-ray diffraction. *Crystal Research-Technology*, 53(2), 1700157. https://doi.org/10.1002/crat.201700157

Kayacı, K. (2020). The use of perlite as flux in the production of porcelain stoneware tiles. *Boletín de la Sociedad Española de Cerámica y Vidrio, 60*(5), 283-290. https://doi.org/10.1016/j.bsecv.2020.03.003

Kawsar, Md., Sahadat, H.Md., Newaz, M.B., Samina, A. (2024). Synthesis of nano-crystallite hydroxyapatites in different media and a comparative study for estimation of crystallite size using Scherrer method, Halder-Wagner method size-strain plot, and Williamson-Hall model. *Heliyon*, 10(3), e25347. https://doi.org/10.1016/j.heliyon.2024.e25347

Kingery, W.D., Bowen, H.K., Uhlmann, D.R. (1976). Introduction to Ceramics (2nd edition). Wiley, 978-0-471-47860-7, 1056.

Koca, K. (2019). Investigation of Vitrified Ceramic Production Supplies from Combinations of Pumice and Industrial Wastes. Thesis (M.Sc.), Atatürk University, Institute of Science and Technology, Türkiye.

Koca, K., Benkli, Y.E. (2025). Microstructural and elemental characterization of pumice–bauxite–clay ceramics: effects of sintering temperature and Scherrer-based analysis. *Journal of the Australian Ceramic Society*. https://doi.org/10.1007/s41779-025-01242-8

Kuzugudenli, O.E. (2004). Use of pumice stone as a ceramic raw material. *Key Engineering Materials*, 264–268, 1427–1430. https://doi.org/10.4028/www.scientific.net/kem.264-268.1427

Kuzugudenli, O.E., Zengin, G. (2004). Production of low-density ceramics using pumice stone. *Key Engineering Materials*, 264–268, 2527–2530.

https://doi.org/10.4028/www.scientific.net/kem.264-268.2527

Liu, K., Shi, Y., Li, C., Hao, L., Liu, J., Wei, Q. (2014). Indirect selective laser sintering of epoxy resin-Al_2O_3 ceramic powders combined with cold isostatic pressing. *Ceramics International*, 40(5), 7099–7106. https://doi.org/10.1016/j.ceramint.2013.12.043

Liu, K., Sun, H., Shi, Y., Liu, J., Zhang, S., Huang, S., Wang, M. (2016). Research on selective laser sintering of Kaolin–epoxy resin ceramic powders combined with cold isostatic pressing and sintering. *Ceramics International*, 42(9), 10711–10718. https://doi.org/10.1016/j.ceramint.2016.03.190

Lu, T. J., & Fleck, N. A. (1998). The thermal shock resistance of solids. *Acta Materialia, 46*(13), 4755–4768. https://doi.org/10.1016/S1359-6454(98)00127-X

Lukianova, O. (2015). Mechanical and elastic properties of new silicon nitride ceramics produced by cold isostatic pressing and free sintering. *Ceramics International*, 41(10A), 13716–13720. https://doi.org/10.1016/j.ceramint.2015.08.026

Mercan, E. (2021). Production of Aerogel-Modified Expanded Perlite Aggregate and Clay (AEP/C) Board and Investigation of Physical and Mechanical Properties. Thesis (M.Sc.), Ihsan Doğramacı Bilkent University, Institute of Economics and Social Sciences, Türkiye.

Monshi, A., Foroughi, M.R., Monshi, M.R. (2012). Modified Scherrer equation to estimate more accurately nano-crystallite size using XRD. *World Journal of Nano Science and Engineering*, 2(3), 154-160. https://doi.org/10.4236/wjnse.2012.23020

Nusrat, J.T., Sahadat, H.Md., Newaz, M.B., Samina, A. (2024). Green synthesis of Ag_2O - facile synthesis of ZnO and characterization using FTIR, bandgap energy - XRD (Scherrer equation, Williamson-Hall, size-train plot, Monshi-Scherrer model). *Results in Chemistry*, 7, 101313. https://doi.org/10.1016/j.rechem.2024.101313

Oztürk, B.Z., Can, A. (2023). Sürdürülebilir endüstriyel özellikleri taşıyan seramik sağlık gereci sırları üretiminde mikronize pomzanın kullanımı. *Gazi Üniversitesi Mühendislik Mimarlık Fakültesi Dergisi*, 38(3), 1967-1978. https://doi.org/10.17341/gazimmfd.1121723

Poyraz, H.B., Erginel, N., Ay, N. (2006). The use of pumice (pumicite) in transparent roof tile glaze composition. *Journal of the European Ceramic Society*, 26(4-5), 741–746. https://doi.org/10.1016/j.jeurceramsoc.2005.06.032

Rahaman, M.N. (2003). Ceramic Processing and Sintering (2nd Edition), CRC Press, 9781315274126, Boca Raton, 875. https://doi.org/10.1201/9781315274126

Reka, A., Pavlovski, B., Lisichkov, K., Jashari, A., Boev, B., Boev, I., Lazarova, M., Eskizeybek, V., Oral, A., Jovanovski, G., Makreski, P. (2019). Chemical, mineralogical and structural features of native and expanded perlite from Macedonia. *Geologia Croatica*, 72(3), 215–221. https://doi.org/10.4154/gc.2019.18

Rzepa, K., Wons, W., Reben, M. (2016). Building ceramics with improved thermal insulation parameters. *E3S Web of Conferences*, 10, 00082. https://doi.org/10.1051/e3sconf/20161000082

Tarhan, M., Tarhan, B. (2018). The Effect of Perlite Use on Ceramic Wall Tile Technical Properties. International *Journal of Engineering Research and Development*, 10(1), 94–100. https://doi.org/10.29137/umagd.364552

Tarhan, B., Tarhan, M. (2022). Utilization of perlite as an alternative raw material in the production of ceramic sanitaryware. *Journal of Thermal Analysis and Calorimetry*, 147, 3509–3518. https://doi.org/10.1007/s10973-021-10784-5

Wang, Q., Sui, J., Li, L., Tuo, Y., Zhang, W., Zhong, G., Zhou, H., & Feng, X. (2024). Recent advances in regulating ceramic monolithic catalyst structure for preferential oxidation of CO in H_2. *Molecules, 29*(15), 3481. https://doi.org/10.3390/molecules29153481

Zhang, S.S. (2006). The effect of the charging protocol on the cycle life of a Li-ion battery. *Journal of Power Sources*, 161(2), 1385–1391. https://doi.org/10.1016/j.jpowsour.2006.06.040